CrossMark

Optical and structural properties of TiO$_2$ nanopowders with Ce/Sn doping at various calcination temperature and time

Mahnaz Alijani[1] · Behzad Koozegar Kaleji[1]

Abstract In this paper, the influence of calcination temperature and time has been investigated on the structural, morphological, optical, and photo-catalytic properties of Sn/Ce co-doped TiO$_2$ nano-powders prepared via sol–gel process. They were calcined at the temperatures in the range of 475–975 °C for 1 and 2 h. The photocatalytic ability of TiO$_2$ powders was evaluated by means of methylene blue degradation experiments conducted under the irradiation of simulated solar light. The X-ray diffraction results showed that the tensile strain in the host lattice was present. The comparison with undoped and Sn or Ce-doped TiO$_2$, co-doped TiO$_2$ shows an obviously higher catalytic activity under visible light irradiation. The absorbance spectrum of Ce and Sn co-doped TiO$_2$ exhibited significant red-shift to visible region. The red-shift is caused by the appearance of a new electronic state in the middle of the TiO$_2$ band-gap. FESEM images show the formation of doped TiO$_2$ nanoparticles with small size in structure and spherical in shape. The FTIR spectra exhibited peaks corresponding to the anatase and rutile structure phases of TiO$_2$.

1 Introduction

Photocatalytic technology is an important method of dealing with environmental pollution in recent years (Liu et al. 2010; Inturi et al. 2014). TiO$_2$-based photocatalysts are widely used for pollution control because they have many advantages such as high photocatalytic,

---

✉ Mahnaz Alijani
  mahnaz.alijani@icloud.com

  Behzad Koozegar Kaleji
  b.kaleji@malayeru.ac.ir; bkaleji@yahoo.com

[1] Department of Materials Engineering, Faculty of Engineering, Malayer University, P.O. Box: 65719-95863, Malayer, Iran

physical and chemical activity, long-term stability against photo and chemical corrosion, low cost, and non-toxicity (Fujishima et al. 2000; Jiang et al. 2015; Chen and Mao 2007). However, the major constraints for TiO_2 photocatalyst are its low quantum efficiency, wide bandgap (3.2 eV) energy, and relatively high electron–hole recombination rate (Lee et al. 2005). Therefore, doping with metals in TiO_2 is becoming essential to increase the life time of the charge carrier as well as band gap tuning to a desired level (Nainani et al. 2012; Zaleska 2008). It has been reported that TiO_2 of a mixed anatase–rutile phase assemblage exhibits superior photocatalytic performance as a result of improved charge carrier separation through the trapping of conduction band electrons in the rutile phase (Ohno et al. 2003; Zhou et al. 2010; Sarkar et al. 2013; Sun and Smirniotis 2003; Kaleji et al. 2016). Lin et al. (1999) and Maruska and Ghosh (1978) have related the higher photoactivity of anatase TiO_2 to its higher Fermi level compared to that of rutile TiO_2. However, high photocatalytic activity has been reported with multi-phased mesoporous TiO_2, consisting of anatase and rutile (Bickley et al. 1991; Yu et al. 2002). Many ionic dopants in different valance state have been investigated, including metallic and nonmetallic ions. Among lanthanide ions, cerium is arguably the most exciting for researchers in the field of photocatalysis. The catalytic activity of ceria attributes to its high oxygen storage capacity which is largely due to two common valence state cerium (III) and cerium (IV). The ability of Ce^{3+} to oxidize to Ce^{4+} states leads to high oxygen mobility which in turn leads to a strong catalytic potential (Ivanova 2009). Particularly TiO_2 doped with Sn has proved to be an effective and widely used method (Li and Zeng 2007). The positive effect of Sn on titania catalytic efficiency was attributed to a change of the anatase electronic structure which decreases the band gap (shift of absorption edge towards visible light) and to the introduction of specific Sn related surface sites (Tripathi et al. 2015; Boppana and Lobo 2011).

Kaleji et al. (2011) have studied the effect of Sn doping in TiO_2 and found that doping of Sn accelerated the transformation from anatase to rutile phase fo TiO_2. The degradation amount of MB increased by increasing Sn dopant (up to 15 mol%).

In our previous research we studied the effect of doping Sn (1–5–10 mol%) and Ce (0.5–1–2 mol%) on photocatalytic behavior of titania based nanoparticles. We found that 5 mol% of Sn and 2 mol% on Ce shows the most significant improvement on photocatalytic behavior of TiO_2 under visible light irradiation (Kaleji et al. 2016). In this paper, the influence of calcination temperature and time was investigated on the structural and optical properties of TiO_2 nanopowders prepared by sol–gel method. The efficiency of these samples as photocatalysts for the degradation of MB, as an organic compound model, under visible light, was investigated.

2 Experimental procedures

2.1 Preparation of the nanopowders

In this paper, the preparation of precursor solution for Sn/Ce co-doped TiO_2 nanoparticles is described as follows: titania, tin oxide and ceria sols were prepared, separately. For the preparation of TiO_2 sol, titanium (IV) butoxide (TBT = $Ti(OC_4H_9)_4$, Aldrich) was selected as titanium source. First, 0.2 mol ethanol (EtOH, Merck) and 0.04 mol ethyl acetoacetate (EAcAc is as a sol stabilizer during preparation of sol, Merck) were mixed, and then 0.01 mol TBT was added by the rate of 1 ml/min to the mixture at the ambient

temperature (25 °C). The solution was continuously stirred for 45 min, followed by the dropping of HNO_3 as catalyst to the solution until pH of 3 is reached.

De-ionized water was added to the solution slowly to initiate hydrolysis process. Solution was aged for 24 h in order to complete all reactions. The chemical composition of the resultant alkoxide solution was $TBT:H_2O:HNO_3:EAcAc:EtOH = 1:10:1:4:20$ in molar ratio. In order to prepare tin oxide sol and ceria sol, stannous chloride ($SnCl_2 \cdot 2H_2O$, Merck) and cerium nitrate hexahydrate ($Ce(NO_3)_3 \cdot 6H_2O$, Merck) were dissolved in EtOH with molar ratio of $SnCl_2 \cdot 2H_2O:EtOH = 1:20$ and $Ce(NO_3)_3 \cdot 6H_2O:EtOH = 1:20$ at ambient temperature with continuous stirring. Solutions were aged for 24 h in order to complete all reactions. Then, mixtures of TiO_2, tin oxide, and ceria sol were made with 2 mol percent of Ce and 5 mol percent of Sn (TSC) at the ambient temperature. Samples were dried up at 100 °C for 1 h. Afterwards, the prepared samples were calcined in air atmosphere at different calcination temperatures ranging from 475 to 975 °C, at a heating rate of 5 °C/min during 1 and 2 h conducted separately.

2.2 Characterization methods

The crystal phases of products were determined by XRD patterns obtained on a Unisantis XMD300 powder diffractometer unit using Cu kα ($\lambda = 1.5418$ Å) at 45 kV and 0.8 Ma using standard sample holder. The samples were scanned in the 2θ ranging of 20°–70°. The average crystallite size of nanopowders (d) was determined from the XRD patterns, according to the Scherrer equation (Kaleji et al. 2016; Ilkhechi et al. 2016).

$$d = k\lambda/\beta\cos\theta \qquad (1)$$

where k is a constant (shape factor, about 0.9), λ the X-ray wavelength (0.154 nm), β the full width at half maximum (FWHM) of the diffraction peak, and θ is the diffraction angle. The values of β and θ of anatase and rutile phases were taken from anatase (101) and rutile (110) planes diffraction lines, respectively. The amount of rutile in the samples was calculated using the following equation (Kaleji et al. 2016; Ilkhechi et al. 2016).

$$X_R = (1 + 0.8(I_A/I_R))^{-1} \qquad (2)$$

where X_R is the mass fraction of rutile in the samples, and I_A and I_R are the X-ray integrated intensities of (101) reflection of the anatase and (110) reflection of rutile, respectively. The diffraction peaks of crystal planes (101), (200), and (105) of anatase phase in XRD patterns were selected to determine the lattice parameters of the TiO_2 and doped TiO_2 nanopowders. The lattice parameters were obtained by using the Eq. 3 (Kaleji et al. 2016; Ilkhechi et al. 2016).

$$\text{(Bragg's law)} : 2d_{(hkl)} \sin\theta = \lambda$$
$$(1/d_{hkl})^2 = (h/a)^2 + (k/b)^2 + (l/c)^2 \qquad (3)$$

where $d_{(hkl)}$ is the distance between the crystal planes of (h k l); λ is the wavelength of X-ray used in the experiment; θ is the diffraction angle of the crystal plane (h k l); h k l is the crystal plane index; and a, b, and c are lattice parameters (in anatase form, $a = b \neq c$).

Fourier transform infrared (FTIR) spectra were recorded using a Perkin-Elmer Spectrum (RXI) spectrophotometer in the range 400–4000 cm^{-1}. Each FTIR spectrum was collected after 20 scans with the resolution of 2 cm^{-1}. Morphology of the nanopowder was observed using the scanning electron microscope (FE-SEM, TESCAN-MIRA3) with an accelerating

voltage of 10–30 kV. The samples used for SEM characterization were coated with 5 nm thin layer of Au using the standard sputtering technique. Nitrogen adsorption isotherms were measured at 77 K using a N_2 adsorption analyzer (Bel Japan-BelSORP miniII). The Brunauer, Emmett, and Teller (BET) model was used to estimate the surface area of the samples according to the N_2 adsorption data.

2.3 Photocatalytic degradation and band gap energy measurement

The visible-light-driven photocatalytic activity of the nanopowders was evaluated by adopting methylene blue (MB) solution (5 ppm) as model pollutant under visible light radiation. The samples were placed in 20 ml aqueous MB solution and prior to the photocatalytic experiment, The reaction mixture solution was initially stirred for about 2 h in a dark environment in order to reach the adsorption equilibrium. Then, they were irradiated using a visible irradiation. The high pressure Mercury vapor lamp (300 W, Osoram) with UV filter was used as a visible light source with 35,000 lm. Cut-off filter was placed in the path of light for the complete removal of UV radiation and running water was circulated around the sample container to filter IR radiation and to keep the reaction mixture at room temperature. Samples were collected at regular irradiation intervals, and the changes in concentration of MB solution were measured using a UV–Vis spectrometer (PerkinElmer spectrometer lambda 25) at wave length of 664 nm (λ_{max}). The activity of catalyst is evaluated by the degradation rate (d) of the samples. The equation of the degradation rate is as followed:

$$d(\%) = (A_0 - A_t)/A_0 \times 100 \tag{4}$$

where d is the degradation percentage, A_0 is the initial absorbance of MB, and A_t is the absorbance of MB after t minutes (Baker 2004).

The optical gap value is estimated relying on the Kubelka–Munk method combined with the Tauc relation:

$$[(\alpha h\nu) = A(h\nu - Eg)^n] \tag{5}$$

where A is a constant which does not depend on photon energy, α is absorption, E_g is the average band gap of the material and "n" depends on the type of transition, n = 2 for direct transmission and n = 1/2 for indirect transmission (Yang et al. 2009), h is the Plank's constant (6.626×10^{-34} J s), and v is the frequency of photons (Guo et al. 2005; Verma et al. 2005; Molea et al. 2012). The direct and indirect average bandgap transition energies were estimated from the intercepts of linear portion of the $(\alpha h\nu)^2$ or $(\alpha h\nu)^{1/2}$ versus hv of plots, respectively.

3 Results and discussion

3.1 X-ray diffraction studies of the nanopowders

Figure 1 shows XRD diffraction patterns of pure and Ce/Sn doped (TC and TS) and co-doped TiO_2 (TSC) nanoparticles calcined at 475 °C for 1 and 2 h. It is appeared that diffraction peaks of the pure and Ce doped TiO_2 samples match closely with those of a standard anatase TiO_2 (JCPDS card number 21-1272) with high crystallinity.
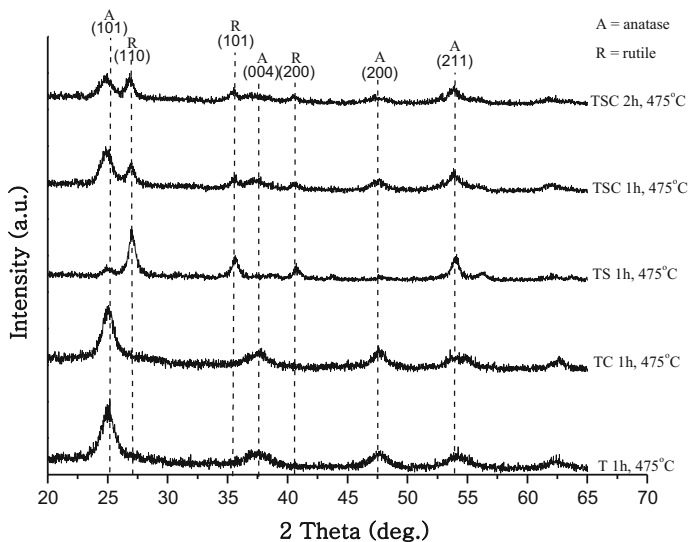
Fig. 1 XRD spectra of the pure and doping TiO$_2$ powders

In the phase composition, anatase appeared as the main phase, and rutile crystallization was promoted by Sn^{4+} doping but was inhibited by Ce^{3+} doping. No signs of metal or oxide phases of Tin or Cerium were detected. This suggests that Sn^{4+} and Ce$^{3+/4+}$ were entered and incorporated in TiO$_2$ lattice (Fresno et al. 2005). The addition of Sn has a positive effect on the transformation of anatase to rutile crystalline phase (Tai and Oh 2002; Kumar et al. 2007), due to the rutile-like structure of SnO$_2$-cassiterite phase. According to the XRD patterns, the crystallite size of TiO$_2$ nanoparticles was determined from the most intense peak (101) of anatase and (110) of rutile using the Scherrer formula. The calculated crystallite size and lattice parameter of anatase and rutile, are reported in Table 1. By comparing the relative intensity of the diffraction peaks, it can be seen that the intensity of (101) plane decreased and the peak position (2θ) decreased with doping. A small shift of diffraction peaks towards the lower angle, and the decrease of peak intensity by doping, indicates that cations are doped into TiO$_2$ crystal lattice successfully. The crystallite size of anatase was 21.8 nm for pure nanoparticles, 12.6 nm for Ce-doped, 13.4 nm for Sn-doped and 10.59 nm for Sn/Ce co-doped heat treatment at 475 °C for 1 h.

3.1.1 Calcination temperature

Figure 2 shows XRD diffraction patterns of pure and Ce/Sn doped (TC and TS) and co-doped TiO$_2$ (TSC) nanoparticles calcined at 475–975 °C for 1 h. The peaks were rather sharp, which indicated relatively high crystallinity. As shown in Table 2, the anatase crystallite size increases with calcination temperature for all catalyst concentrations. As the temperature increases the atoms gain sufficient energy for diffusive motion and thereby increasing the crystallite size (Yang et al. 2007). The average crystalline size calculated by applying the Scherrer formula on the anatase (101) diffraction peak was 21.8, 10.59, 11.83, 14.49 nm for the pure TiO$_2$-475, TSC-475, TSC-575, and TSC-675 samples (shown in Table 2), and on the rutile (110) diffraction peak was 14.87, 24.38, 25.71, 42.35, 46.25, 58.16 nm for TSC-475, TSC-575 and TSC-675, TSC-775, TSC-875 and TSC-975

Table 1 The characteristic of nano powders after thermal treatment at 475 °C

Sample	% Anatase	% Rutile	$d_{Anatase}$ (nm)	d_{Rutile} (nm)	a = b (Å)	c (Å)	$V_{u.c}$ (Å)^3	Surface area BET ($m^2 g^{-1}$)
T-1 h-475	100	–	21.8	–	3.822	10.660	155.717	71.488
TC-1 h-475	100	–	12.6	–	3.813	9.359	136.07	123.685
TS-1 h-475	14	86	13.4	14.1	4.647	3.983	86.011	102.221
TSC-1 h-475	62	38	10.59	14.87	3.801	9.528	137.656	122.732
TSC-2 h-475	39	61	9.62	19.27	4.426	3.073	60.198	71.797

respectively. The average crystalline size increases as the calcination temperature increases. As the temperature further increases to 975 °C, the anatase phase completely transforms into the rutile phase. The diffraction peaks at 2θ angle 25°, 37.5° and 47.1° corresponding respectively to diffraction from planes (101), (004), and (200) of TiO_2 at high temperature decreased or were removed. There was an additional peak in XRD patterns of the Sn/Ce co-doped sample calcined at 975 °C, indicating the formation of SnO_2 as illustrated in Fig. 2.

3.1.2 Calcination time

Besides temperature, calcination time also has important impact on structure and properties of the prepared TiO_2 nanopowders, as illustrated in Fig. 3. The characteristics of all samples after thermal treatment at 475–775 °C for 2 h periods are reported at Table 3. The peak situated at 2θ 25.3° is the strongest diffraction peak representing (101) plane of anatase TiO_2 and (110) plane of rutile TiO_2. As the temperature increased, the intensities of the anatase peaks were increased indicating an improvement in crystallinity, and also the
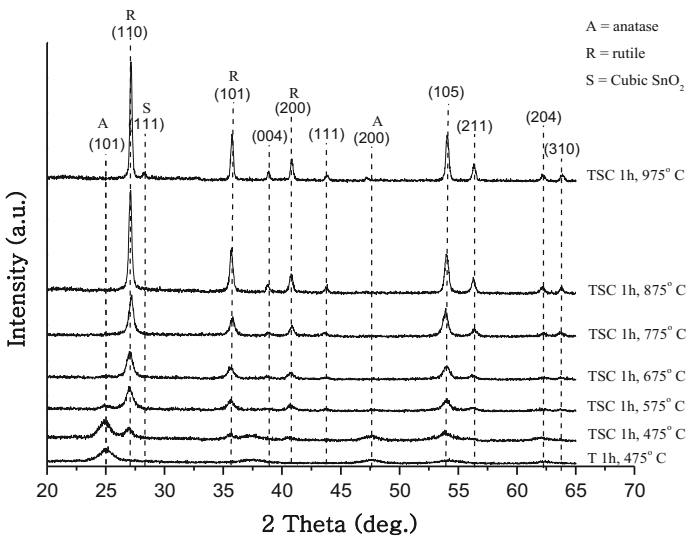

Fig. 2 XRD patterns of pure TiO_2 and Ce/Sn co-doped TiO_2 powders, formed at various temperature 475–975 °C for 1 h

Table 2 The characteristic of nano powders as prepared at 475–975 °C for 1 h

Sample	% Anatase	% Rutile	d$_{Anatase}$ (nm)	d$_{Rutile}$ (nm)	a = b (Å)	c (Å)	V$_{u.c}$ (Å)^3	Surface area BET (m^2 g^{-1})
T	100	–	21.8	–	3.822	10.660	155.717	71.488
TSC-1 h-475	62	38	10.59	14.87	3.801	9.528	137.656	122.732
TSC-1 h-575	13	87	11.83	24.38	4.427	3.059	70.358	62.828
TSC-1 h-675	4	96	14.49	25.71	4.426	3.060	70.522	56.099
TSC-1 h-775	–	100	–	42.35	4.413	3.049	59.377	33.335
TSC-1 h-875	–	100	–	46.25	2.981	2.981	67.372	30.524
TSC-1 h-975	–	100	–	58.16	2.995	2.995	64.481	24.273

intensities of the anatase peaks decreased, but the rutile peaks appeared. The diffraction peak intensity of anatase TiO$_2$ was lowered with extending the calcination time from 1 to 2 h.

3.2 FE-SEM analysis of pure and doped TiO$_2$ nanopowders

Morphologies of Sn/Ce co-doped TiO$_2$ calcined at 475, 575, 775 °C are illustrated by FE-SEM micrographs and presented in Fig. 4. By increasing the temperature, particles become larger and longer. The aggregation of TiO$_2$ nanoparticles resulted by increasing the temperature was observed, as shown in Fig. 4c. It can be seen from Fig. 4d that calcination time has noticeable effect on morphology of TiO$_2$ powders. It can be clearly seen that the microstructures of the powders are strongly affected by calcination time and temperatures due to aggregation of particles' size. The doped TiO$_2$ samples are composed of strongly agglomerated Nanometric particles, island-like in shape.
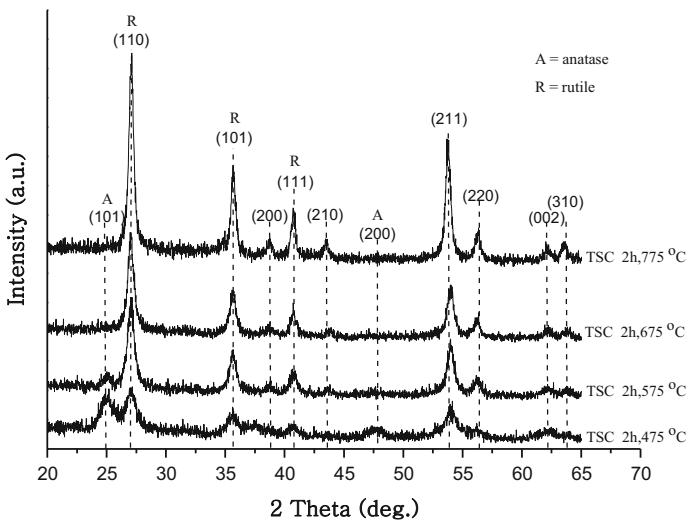

Fig. 3 XRD patterns of Ce/Sn co-doped TiO$_2$ powders, formed at various temperature 475–775 °C for 2 h

Table 3 The characteristic of nano powders as prepared at 475–975 °C for 2 h

Sample	% Anatase	% Rutile	$d_{Anatase}$ (nm)	d_{Rutile} (nm)	a = b (Å)	c (Å)	$V_{u.c}$ (Å)^3	Surface area BET (m^2 g^{-1})
TSC-2 h-475	39	61	9.62	19.27	4.426	3.073	60.198	71.797
TSC-2 h-575	9	91	15.43	23.02	4.426	3.119	61.099	64.406
TSC-2 h-675	–	100	–	32.01	4.426	3.059	59.924	44.103
TSC-2 h-775	–	100	–	47.12	4.426	3.053	59.806	29.961

3.3 Fourier transform infrared (FTIR) studies

Figure 5 shows the FT-IR spectra of pure TiO_2 and Ce/Sn co doped TiO_2 calcined at 475 °C in the range of 400–4000 cm^{-1}. These spectra showed the vibrations of the various groups at different wavelengths of IR radiation. A broad peak at 3413 cm^{-1}, is the result of O–H stretching modes which originate from the surface water molecules; These are related to the physical absorption of water in TiO_2 nanoparticles (Johnson 1973; Mul 2001; Du et al. 2008). A broad peak can be seen at 3433 cm^{-1}, assigned to stretching vibration mode of OH groups and the symmetric and antisymmetric OH modes of molecular water with in TiO_2 nanoparticles (Johnson 1973; Mul 2001; Du et al. 2008). The bending vibration corresponding to the molecular water bending band is observed at 1624 cm^{-1}. The TiO_2– OH bonds arise from the hydrolysis reaction. While the narrow bands at 2929 and 2852 cm^{-1} are due to organic residues originating from the sample as a result of the preparation procedure. The band at 1468 cm^{-1} is due to the in-plane skeletal vibrations of aromatic rings. The broad intense band seen below 1200 cm^{-1} is due to Ti–O–Ti vibrations (Ganesh et al. 2012a, b). In the low energy region of the spectrum the bands at 523 and 495 cm^{-1} are assigned to bending vibrations of Ti–O and Ti–O–Ti framework bonds (Maira et al. 2001). The shift of the main adsorption at 490 cm^{-1} and the increased intensity of the band near 828 cm^{-1} are generally attributed to the transformation of anatase to rutile crystal phase. The main absorptions noted in the two samples are associated with the phase transformed TiO_2 nanoparticles (National Bureau of Standards 1969). These results match very well with those reported in the literature for Sn and Ce doped TiO_2 powders and for anatase and rutile phases of TiO_2 (Ganesh et al. 2012a, b; Chen et al. 2009).

3.4 Optical evaluation

It is established that TiO_2 has direct and indirect band gaps. (Janitabar-Darzi et al. 2009) To determine values of these forbidden energies, the absorption data were fitted to the Tauc relation (Eq. 5) for indirect and direct band-gap transitions. A quantitative evaluation of the band gap energy (E_g) can be performed by plotting $(\alpha h\nu)^{1/2}$ versus hc and extrapolated from linear part of the curve as shown in Fig. 6. Figure 7 shows the $(\alpha h\nu)^{1/2}$ versus hν for α indirect transition and Fig. 6 shows the $(\alpha h\nu)^2$ versus hν for α direct transition. When a semiconductor absorbs photons of energy larger than the gap of the semiconductor, an electron is transferred from the valence band to the conduction band where there occurs an abrupt increase in the absorbency of the material to the wavelength corresponding to the band gap energy. The relation of the absorption coefficient (α) to the incidental photon energy depends on the type of electronic transition. When, in this transition, the electron
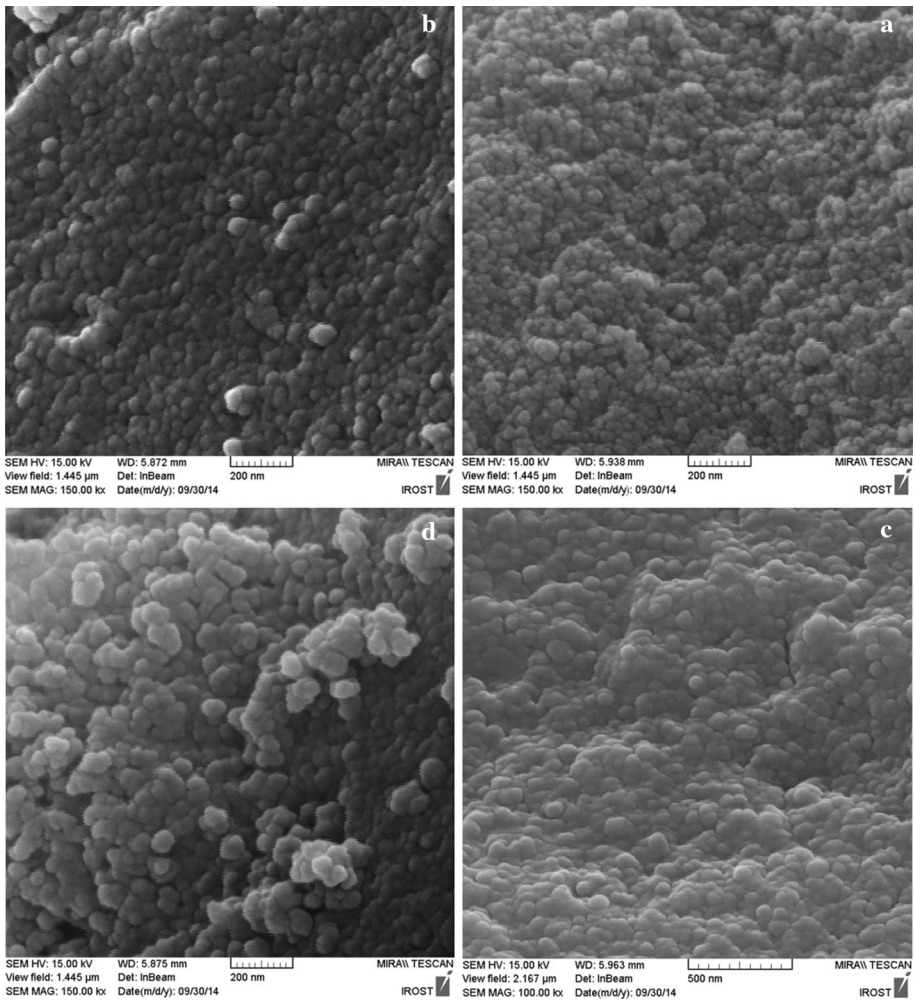
Fig. 4 FE-SEM images of pure (**a**) and co-doped TiO$_2$, calcination temperature at 475 °C (**b**) for 1 h, 675 °C (**c**) for 1 h, 775 °C (**d**) for 1 h, 775 °C (**e**) for 2 h

momentum is conserved, the transition is direct, but if the momentum does not conserve this transition, it must be attended by a photon, this is an indirect transition (Cao et al. 2009). The allowed indirect optical absorption of the TiO$_2$ band gap at about 3.2 eV (Fig. 6) for the indirect optical absorption and at 3.25 eV value for the direct optical absorption (Fig. 7) were then found, respectively. As represented in these figures, we found that the band gap values for the direct transition are higher than indirect transition.

Doping Sn^{4+} has been found to be located approaching and below the conduction band (Valencia et al. 2010). Therefore, the red-shift of the absorption edge for the Sn-doped TiO$_2$ should be the result of the electronic transition from the valence band to the doping energy level. On the other hand, according to the XRD results, doping with Sn accelerated the transformation from anatase to rutile phase of TiO$_2$, and the rutile phase has a band gap smaller than that of anatase, so this transformation should be another reason for the red-
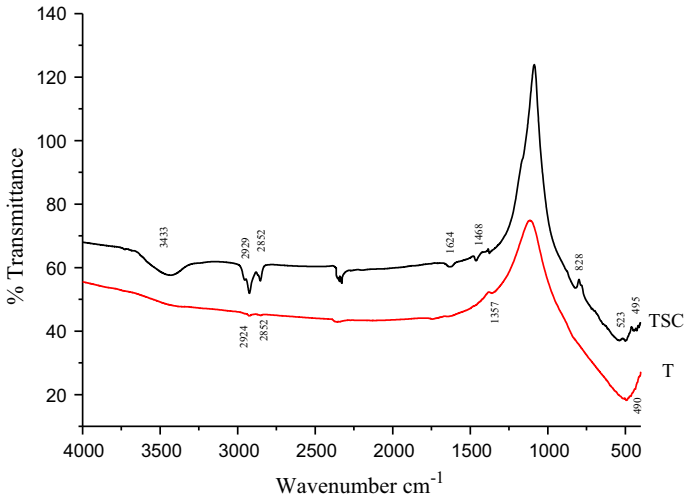
Fig. 5 FTIR spectra for the as-prepared undoped TiO_2 and Sn/Ce co-doped TiO_2 calcination temperature at 475 °C

shift. When Ce was introduced into the samples, the red-shift of absorption occurred, which implied a decrease in the band gap energy. It can also be seen that Sn/Ce co-doped catalyst showed the largest red-shift among all doped catalysts. This indicated that the electrons in the valence band could more easily move into the conduction band and therefore generate electron–hole pairs, which might be beneficial to improve the redox properties of the catalysts.

3.5 Photocatalytic degradation of MB

Figure 8a shows the normalized concentration at 664 nm absorption of the MB solutions separated from the TiO_2 nanopowders as a photocatalyst under various time irradiations (0–120 min) to determine the photo-catalytic degradation under the visible light irradiation. Figure 8b shows the results of photo-catalytic decomposition of MB solution caused
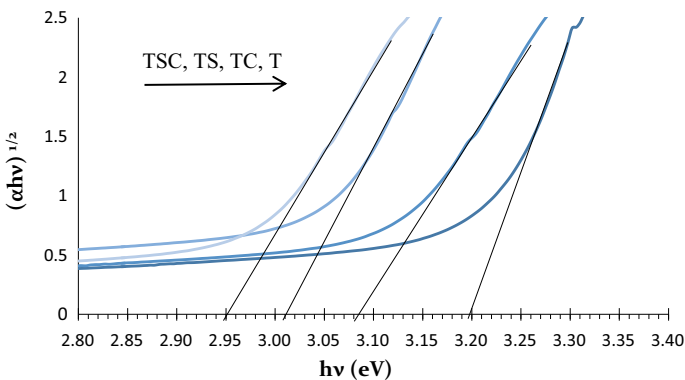

Fig. 6 Tauc plots of pure and doped TiO_2 nanopowders calcined at 475 °C for 1 h. (indirect bandgap energy)
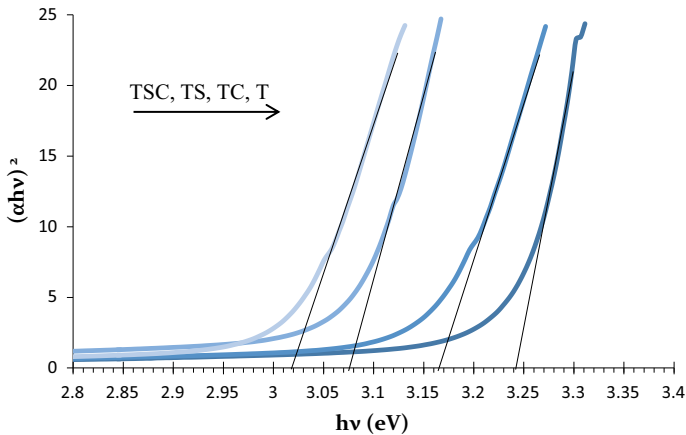
Fig. 7 Tauc plots of pure and doped TiO$_2$ nanopowders calcined at 475 °C for 1 h. (direct bandgap energy)

by degradation of MB in contact with different samples. According to Fig. 8, the order of photo-catalytic activity of TiO$_2$ nanopowders at 60 min under the visible irradiation was as following: TSC > TS > TC > T, which suggests that the co-doping enhances the photo-catalytic activity of pure and single doped TiO$_2$. This enhanced photocatalytic activity is because of suppressed recombination of photo generated electrons and holes.

Figures 9, 10 shows the results of photo-catalytic decomposition of MB solution caused by degradation of MB in contact with nanopowders with Sn and Ce dopants at different calcination time and temperatures. Highest photo degradation of MB is for the TSC sample calcined at temperature of 675 °C for 1 h. When the calcination temperature of co-doped TiO$_2$ increased to 675 °C the photocatalytic reaction rate tends to increase and then decreased at higher calcination temperature, because at high calcination temperature samples have rutile structure and gave lower degradation efficiency compared with the samples calcined at lower temperatures. The photocatalytic activity of TiO$_2$ generally increased with increasing crystallization and decreased with decreasing surface area. Higher calcination temperature could promote the crystallization of TiO$_2$ and effectively remove the bulk defects sites for the recombination of the photo-induced electron–hole pairs (Jung and Park 1999). However, when the calcination temperature was increase, surface area of TiO$_2$ would decrease because of aggregation of particles. The combination of crystallization and surface area affected the visible photo-activity of Ce and Sn co-doped TiO$_2$.

3.6 Mechanism of interfacial charge transfer

Figure 11 shows why Ce/Sn co-doped TiO$_2$ exhibits an improved photocatalytic activity over the undoped TiO$_2$ under visible light irradiation.

Introduction of doping levels inside the bandgap can suppress the recombination of photo-generated charge carriers (Cao et al. 2004; Cong et al. 2007). The conduction band (CB) and the valence band (VB) of TiO$_2$ matrix are primarily comprised of Ti (3d) and O (2p) orbitals, respectively (Shough et al. 2009). When additional ions are introduced into the lattice, interaction between the outer-shell orbitals of these ions and the energy states in the bands creates impurity levels and changes the band structures. The influence of the
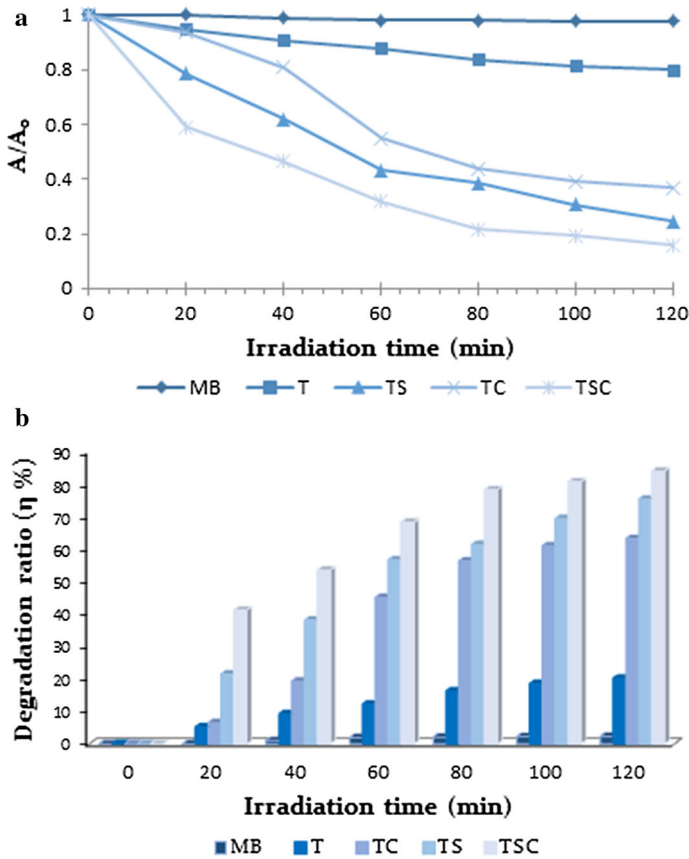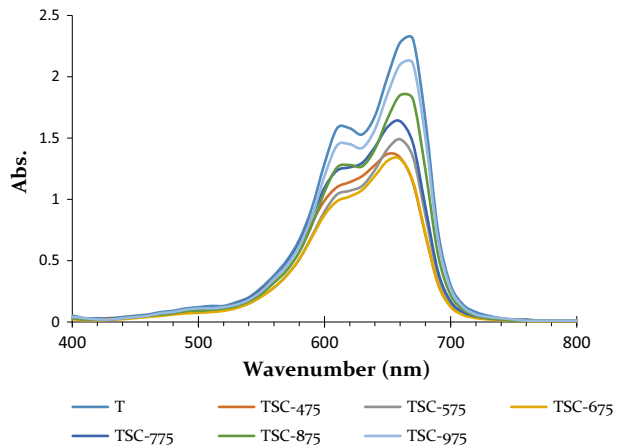
Fig. 8 a Photocatalytic degradation of MB as a function of irradiation time over different prepared TiO$_2$ photocatalysts for different time intervals, **b** MB removals in the photodegradation (η%)

Fig. 9 UV–Vis absorption spectra of pure and co-doped TiO$_2$ nanoparticles calcined at 475 °C) with calculated energy band gaps of samples
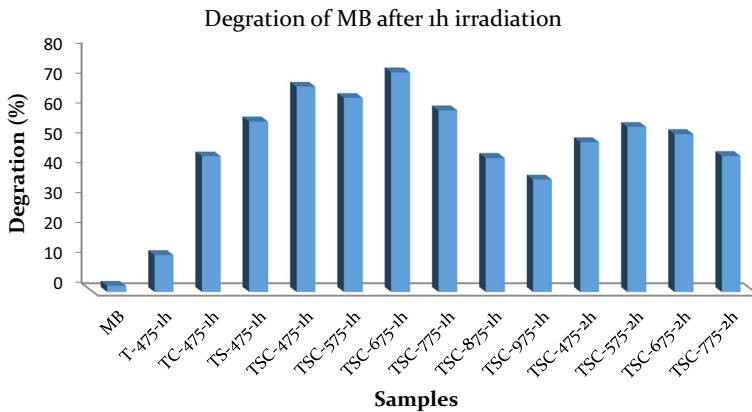
Degration of MB after 1h irradiation

Fig. 10 Photocatalytic degradation of MB determined by pure and doped TiO$_2$ nanopowders at various calcination time and temperature after 60 min visible irradiation
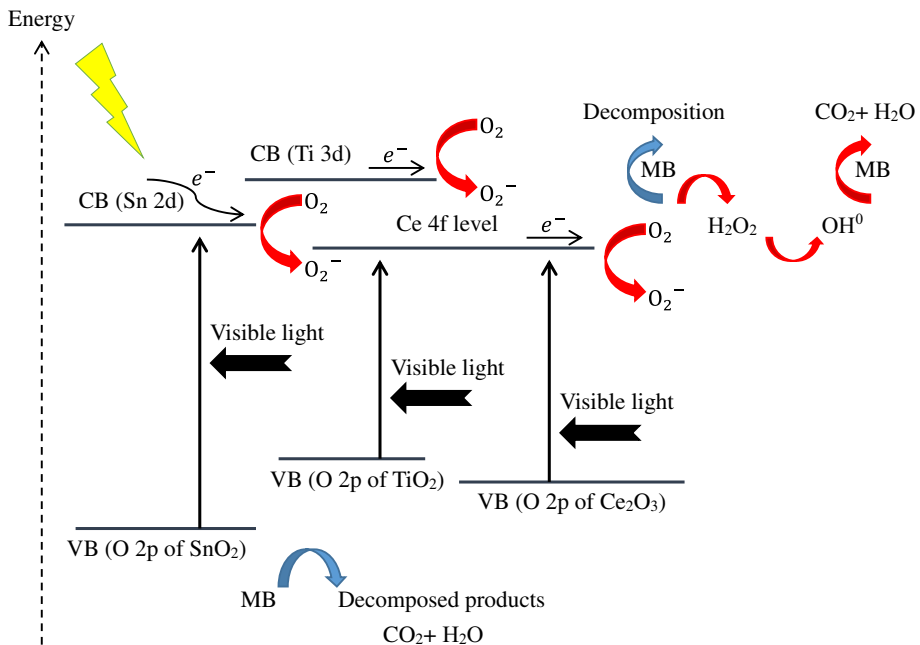

Fig. 11 The proposed valence band structure of Sn and Ce co-dpoed TiO$_2$ and the mechanisms of photoresponse under visible light and photogenerated electron transfer in Ce^{3+}/Sn^{4+}/TiO$_2$/MB system

dopants on the electronic structures is associated with their atomic numbers, ionic radii and oxidation states (Shough et al. 2009; Chang and Liu 2014). It is known that Ce (E$_{CB}$ = −0.54 V) induces unoccupied 4f states just under the TiO$_2$ CB (Chen et al. 2010; Channei and Phanichphant 2014). The electron of Ce–TiO$_2$ was directly irradiated to Ce 4f level under visible light illumination. For Ce^{3+}/TiO$_2$, the Ce 4f level plays an important role in interfacial charge transfer and elimination of electron–hole recombination (Li et al.

2005). As illustrated in XRD results, Sn^{4+} and $Ce^{3+/4+}$ ions are incorporated in TiO_2 lattice in substitution mode. It creates Sn^{4+} doping energy level which is located at 0.4 eV below the conduction band (Wang et al. 2011). The excited electrons transfer from valence band to Sn^{4+} doping energy level. The excited electron at the conduction band can also fall into Sn^{4+} doping energy level (Cao et al. 2004). The photo-generated electrons can also transfer from conduction band to SnO_2 nanoparticles since the conduction band of SnO_2 ($E_{CB} = 0$ V) is lower than that of the TiO_2 ($E_{CB} = -0.5$ V) (Sim et al. 2014).

4 Conclusions

This research focused on the effect of calcination temperature and time Tin/Cerium dopants on phase transformation, crystallite size, and photo-catalytic activity of titania nanopowders. Pure and Sn/Ce doped TiO_2 powders were prepared by sol–gel process and were calcined at temperatures ranging from 475 to 975 °C in air for 1 and 2 h.

The TiO_2 nanopowders calcined at temperatures from 475 to 675 °C are anatase and rutile phase, and further into the rutile phase at 775 °C.

The size of the crystallites in doped TiO_2 samples is smaller than those in undoped sample suggesting that dopants have an inhibiting role on the grain growth. The crystallite size of the powders is increased with increasing calcination temperature and time. According to FE-SEM micrographs, all powders fabricated are uniform, and their crystallinity are increased with increasing calcination temperature and time. The UV–visible measurement reveals a good absorption of the visible light irradiation after doping and a smaller band gap than that of undoped TiO_2. The co-operation of Sn and Ce led to the more narrowing of the band gap and also promoted the separation of the photo-generated electrons and holes. The photocatalytic activity of Sn/Ce co-doped TiO_2 samples strongly depends on the calcination temperature.

References

Baker, R.W.: Membrane technology and application. Wiley Pub, Chichester (2004)

Bickley, R.I., Gonzalez-Carreno, T., Lees, J.S., Palmisano, L., Tilley, R.J.: Structural investigation of titanium dioxide photocatalysts. J. Solid State Chem. **92**, 178–190 (1991)

Boppana, V.B.R., Lobo, R.F.: Photocatalytic degradation of organic molecules on mesoporous visible-light-active Sn (II)-doped titania. J. Catal. **281**, 156–168 (2011)

Cao, Y., Yang, W., Zhang, W., Liu, G., Yue, P.: Improved photocatalytic activity of Sn^{4+} doped TiO_2 nanoparticulate films prepared by plasma-enhanced chemical vapor deposition. New J. Chem. **28**, 218–222 (2004)

Cao, Y., He, T., Zhao, L., Wang, E., Yang, W., Cao, Y.: Structure and phase transition behavior of Sn^{4+}-doped TiO_2 nanoparticles. J. Phys. l Chem. C. **113**, 18121–18124 (2009)

Chang, S.M., Liu, W.S.: The roles of surface-doped metal ions (V, Mn, Fe, Cu, Ce, and W) in the interfacial behavior of TiO_2 photocatalysts. Appl. Catal. B: Environ. **156**, 466–475 (2014)

Channei, D., Phanichphant, S.: $Fe_3O_4/SiO_2/CeO_2$ core–shell magnetic nanoparticles as photocatalyst. J. Nanosci. Nanotechnol. **14**, 7756–7762 (2014)

Chen, X., Mao, S.S.: Titanium dioxide nanomaterials: synthesis, properties, modifications, and applications. Chem. Rev. **107**, 2891–2959 (2007)

Chen, S.W., Lee, J.M., Lu, K.T., Pao, C.W., Lee, J.F., Chan, T.S., & Chen, J.M.: Band-gap narrowing of TiO₂ doped with Ce probed with X-ray absorption spectroscopy. Appl. Phys. Lett **97**, 1–3 (2010)

Chen, Q., Jiang, D., Shi, W., Wu, D., Xu, Y.: Visible-light-activated Ce–Si co-doped TiO₂ photocatalyst. Appl. Sur. Sci. **255**, 7918–7924 (2009)

Cong, Y., Zhang, J., Chen, F., Anpo, M.: Synthesis and characterization of nitrogen-doped TiO₂ nanophotocatalyst with high visible light activity. J. Phys. Chem. C **111**, 6976–6982 (2007)

Du, P., Bueno-Lopez, A., Verbaas, M., Almeida, A.R., Makkee, M., Moulijn, J.A., Mul, G.: The effect of surface OH-population on the photocatalytic activity of rare earth-doped P25-TiO₂ in methylene blue degradation. J. Catal. **260**, 75–80 (2008)

Fresno, F., Coronado, J.M., Tudela, D., Soria, J.: Influence of the structural characteristics of Ti₁₋ₓSnₓO₂ nanoparticles on their photocatalytic activity for the elimination of methylcyclohexane vapors. Appl. Catal. B Environ. **55**, 159–167 (2005)

Fujishima, A., Rao, T.N., Tryk, D.A.: Titanium dioxide photocatalysis. J. Photochem. Photobiol. C Chem Rev. **1**, 1–21 (2000)

Ganesh, I., Gupta, A. K., Kumar, P. P., Sekhar, P. S. C., Radha, K., Padmanabham, G., & Sundararajan, G.: Preparation and characterization of Ni-doped TiO₂ materials for photocurrent and photocatalytic applications. Sci. World J. 1–16 (2012)

Ganesh, I., Gupta, A.K., Kumar, P.P., Sekhar, P.C., Radha, K., Padmanabham, G., Sundararajan, G.: Preparation and characterization of Co-doped TiO₂ materials for solar light induced current and photocatalytic applications. Mater. Chem. Phys. **135**, 220–234 (2012)

Guo, B., Liu, Z., Hong, L., Jiang, H.: Sol gel derived photocatalytic porous TiO₂ thin films. Surf. Coat. Technol. **198**, 24–29 (2005)

Ilkhechi, N.N., Alijani, M., Kaleji, B.K.: Optical and structural properties of TiO₂ nanopowders with Co/Ce doping at various temperature. Opt. Quant. Electron. **48**, 1–9 (2016)

Inturi, S.N.R., Boningari, T., Suidan, M., Smirniotis, P.G.: Visible-light-induced photodegradation of gas phase acetonitrile using aerosol-made transition metal (V, Cr, Fe Co, Mn, Mo, Ni, Cu, Y, Ce, and Zr) doped TiO2. Appl. Catal. B Environ. **144**, 333–342 (2014)

Ivanova, A.S.: Physicochemical and catalytic properties of systems based on CeO₂. Kin. Catal. **50**, 797–815 (2009)

Janitabar-Darzi, S., Mahjoub, A.R., Nilchi, A.: Investigation of structural, optical and photocatalytic properties of mesoporous TiO₂ thin film synthesized by sol–gel templating technique. Physica E **42**, 176–181 (2009)

Jiang, B., Jiang, L., Shi, X., Wang, W., Li, G., Zhu, F., Zhang, D.: Ag₂O/TiO₂ nanorods heterojunctions as a strong visible-light photocatalyst for phenol treatment. J. Sol-Gel. Sci. Technol. **73**, 314–321 (2015)

Johnson, K.H.: Scattered-wave theory of the chemical bond. Adv. Quant. Chem. **7**, 143–185 (1973)

Jung, K.Y., Park, S.B.: Anatase-phase titania: preparation by embedding silica and photocatalytic activity for the decomposition of trichloroethylene. J. Photochem. Photobiol. A: Chem. **127**, 117–122 (1999)

Kaleji, B.K., Sarraf-Mamoory, R., Nakata, K., Fujishima, A.: The effect of Sn dopant on crystal structure and photocatalytic behavior of nanostructured titania thin films. J. Sol-Gel. Sci. Technol. **60**, 99–107 (2011)

Kaleji, B.K., Alijani, M., Aghaei, A.: Sn/Ce co-doping of TiO₂ nanoparticles: influence of dopants concentration on optical and structural characteristics. J. Mater. Sci.: Mater. Electron. **27**, 8524–8531 (2016)

Kumar, K.N.P., Fray, D.J., Nair, J., Mizukami, F., Okubo, T.: Enhanced anatase-to-rutile phase transformation without exaggerated particle growth in nanostructured titania–tin oxide composites. Scripta Mater. **57**, 771–774 (2007)

Lee, M.S., Hong, S.S., Mohseni, M.: Synthesis of photocatalytic nanosized TiO₂–Ag particles with sol–gel method using reduction agent. J. Mol. Catal. A Chem. **242**, 135–140 (2005)

Li, J., Zeng, H.C.: Hollowing Sn-doped TiO₂ nanospheres via Ostwald ripening. J. Am. Chem. Soc. **129**, 15839–15847 (2007)

Li, F.B., Li, X.Z., Hou, M.F., Cheah, K.W., Choy, W.C.H.: Enhanced photocatalytic activity of Ce³⁺–TiO₂ for 2-mercaptobenzothiazole degradation in aqueous suspension for odour control. Appl. Catal. A **285**, 181–189 (2005)

Lin, J., Jimmy, C.Y., Lo, D., Lam, S.K.: Photocatalytic activity of rutile Ti₁₋ₓSnₓO₂ solid solutions. J. Catal. **183**, 368–372 (1999)

Liu, G., Wang, L., Yang, H.G., Cheng, H.M., Lu, G.Q.M.: Titania-based photocatalysts crystal growth, doping and heterostructuring. J. Mater. Chem. **20**, 831–834 (2010)

Maira, A.J., Coronado, J.M., Augugliaro, V., Yeung, K.L., Conesa, J.C., Soria, J.: Fourier transform infrared study of the performance of nanostructured TiO₂ particles for the photocatalytic oxidation of gaseous toluene. J. Catal. **202**, 413–420 (2001)

Maruska, H.P., Ghosh, A.K.: Photocatalytic decomposition of water at semiconductor electrodes. Sol. Energy **20**, 443–458 (1978)

Molea, A., Popescu, V., Rowson, N.A.: Effects of I-doping content on the structural, optical and photo-catalytic activity of TiO_2 nanocrystalline powders. Powder. Techol. **230**, 203–211 (2012)

Mul, G., Zwijnenburg, A., van der Linden, B., Makkee, M., Moulijn, J.A.: Stability and selectivity of Au/TiO_2 and Au/TiO_2/SiO_2 catalysts in propene epoxidation: an in situ FT-IR study. J. Catal. **201**, 128–137 (2001)

Nainani, R., Thakur, P., Chaskar, M.: Synthesis of silver doped TiO_2 nanoparticles for the improved photocatalytic degradation of methyl orange. J. Mater. Sci. B **2**, 52–58 (2012)

National Bureau of Standards, Monograph. **25**, Sec. 7, 83, (1969)

Ohno, T., Tokieda, K., Higashida, S., Matsumura, M.: Synergism between rutile and anatase TiO_2 particles in photocatalytic oxidation of naphthalene. Appl. Catal. A **244**, 383–391 (2003)

Sarkar, D., Mukherjee, S., Chattopadhyay, K.K.: Synthesis, characterization and high natural sunlight photocatalytic performance of cobalt doped TiO_2 nanofibers. Phys. E **50**, 37–43 (2013)

Shough, A.M., Doren, D.J., Ogunnaike, B.: Transition metal substitution in ETS-10: DFT calculations and a simple model for electronic structure prediction. Chem. Mater. **21**, 1232–1241 (2009)

Sim, L.C., Ng, K.W., Ibrahim, S., Saravanan, P.: Synthesis, features and solar-light-driven photocatalytic activity of TiO_2 nanotube arrays loaded with SnO_2. J. Nano. Sci. Tech. **14**, 7001–7009 (2014)

Sun, B., Smirniotis, P.G.: Interaction of anatase and rutile TiO_2 particles in aqueous photooxidation. Catal. Today **88**, 49–59 (2003)

Tai, W.P., Oh, J.H.: Fabrication and humidity sensing properties of nanostructured TiO_2–SnO_2 thin films. Sens. Actuators B Chem. **85**, 154–157 (2002)

Tripathi, A.K., Mathpal, M.C., Kumar, P., Singh, M.K., Soler, M.A.G., Agarwal, A.: Structural, optical and photoconductivity of Sn and Mn doped TiO_2 nanoparticles. J. Alloys Compd. **622**, 37–47 (2015)

Valencia, S., Marín, J.M., Restrepo, G.: Study of the bandgap of synthesized titanium dioxide nanoparticules using the sol–gel method and a hydrothermal treatment. Open Mater. Sci. J. **4**, 9–14 (2010)

Verma, A., Samanta, S.B., Bakhshi, A.K., Agnihotry, S.A.: Effect of stabilizer on structural, optical and electrochemical properties of sol–gel derived spin coated TiO_2 films. Sol. Energy Mater. Sol. Cells **88**, 47–64 (2005)

Wang, E., He, T., Zhao, L., Chen, Y., Cao, Y.: Improved visible light photocatalytic activity of titania doped with tin and nitrogen. J. Mater. Chem. **21**, 144–150 (2011)

Yang, Z., Xu, J., Zhang, W., Liu, A., Tang, S.: Controlled synthesis of CuO nanostructures by a simple solution route. J. Solid State Chem. **180**, 1390–1396 (2007)

Yang, H.M., Zhang, X.C., Tao, Q.F.: Synthesis and characterization of sol–gel derived TiO_2 thin films: effect of different pretreatment process. Inorg. Mater. **45**, 1139–1145 (2009)

Yu, J., Jimmy, C.Y., Ho, W., Jiang, Z.: Effects of calcination temperature on the photocatalytic activity and photo-induced super-hydrophilicity of mesoporous TiO_2 thin films. New J. Chem. **26**, 607–613 (2002)

Zaleska, A.: Doped-TiO_2. A review. Recent Pat. Eng. **2**, 157–164 (2008)

Zhou, W., Liu, Q., Zhu, Z., Zhang, J.: Preparation and properties of vanadium-doped TiO_2 photocatalysts. J. Phys. D Appl. Phys. **43**, 1–7 (2010)